



# Investigation of Inclusion States of Silicate and Carbonate Ions in Hydroxyapatite Particles Prepared under the Presence of Sodium Silicate

Tania Guadalupe Peñafior Galindo <sup>1</sup>, Kazuto Sugimoto <sup>2</sup>, Shota Yamada <sup>2</sup>, Taito Sugibuchi <sup>2</sup>, Zizhen Liu <sup>2</sup> and Motohiro Tagaya <sup>2,\*</sup>

<sup>1</sup> Department of General Education, National Institute of Technology, Nagaoka College, 888 Nishikatakai, Nagaoka 940-8532, Niigata, Japan; taniap@nagaoka-ct.ac.jp

<sup>2</sup> Department of Materials Science and Technology, Nagaoka University of Technology, Kamitomioka 1603-1, Nagaoka 940-2188, Niigata, Japan; k\_sugimoto@stn.nagaokaut.ac.jp (K.S.); shota\_yamada@mst.nagaokaut.ac.jp (S.Y.); sugibuchi0315@gmail.com (T.S.); zizhen\_liu@stn.nagaokaut.ac.jp (Z.L.)

\* Correspondence: tagaya@mst.nagaokaut.ac.jp

**Abstract:** Biological hydroxyapatite (HA) contains the different minor ions which favour its bio-reactivity in vivo. In this study, the preparation of HA particles containing both silicate and carbonate ions under the presence of sodium silicate was investigated, and the physicochemical properties were evaluated according to the contents and states of silicate and carbonate ions. The increment in the silicate ion reduced the crystallinity and expanded the crystalline size along with *a*-axis. Solid-state <sup>29</sup>Si-NMR spectra indicated the increase in the adsorption of oligomeric silicate species on the HA particle surfaces in addition to the substitution state of silicate ions, suggesting the occurrence of the surface coating of silicates on the surfaces. The possible states of carbonate and silicate ions at the HA surfaces will provide the bioactivity.

**Keywords:** hydroxyapatite; nanoparticles; silicate ion reaction; oligomeric silicates; solid-state <sup>29</sup>Si-NMR



**Citation:** Peñafior Galindo, T.G.; Sugimoto, K.; Yamada, S.; Sugibuchi, T.; Liu, Z.; Tagaya, M. Investigation of Inclusion States of Silicate and Carbonate Ions in Hydroxyapatite Particles Prepared under the Presence of Sodium Silicate. *Biomimetics* **2022**, *7*, 40. <https://doi.org/10.3390/biomimetics7020040>

Academic Editor: Stanislav N. Gorb

Received: 18 March 2022

Accepted: 30 March 2022

Published: 1 April 2022

**Publisher's Note:** MDPI stays neutral with regard to jurisdictional claims in published maps and institutional affiliations.



**Copyright:** © 2022 by the authors. Licensee MDPI, Basel, Switzerland. This article is an open access article distributed under the terms and conditions of the Creative Commons Attribution (CC BY) license (<https://creativecommons.org/licenses/by/4.0/>).

## 1. Introduction

The similarity in composition and structure of hydroxyapatite (HA, Ca<sub>10</sub>(PO<sub>4</sub>)<sub>6</sub>(OH)<sub>2</sub>) to the inorganic phase of bones and teeth and its biocompatibility allow it to be used for biomedical applications [1,2]. The low-crystalline HA is suitable for ion substitution in both calcium (Ca<sup>2+</sup>) and phosphate (PO<sub>4</sub><sup>3-</sup>) ions due to its labile crystal structure [3]. The biological HA usually contains the different minor ions such as Na<sup>+</sup>, K<sup>+</sup>, Mg<sup>2+</sup>, Sr<sup>2+</sup>, F<sup>-</sup>, Cl<sup>-</sup>, carbonate (CO<sub>3</sub><sup>2-</sup>), and silicate (SiO<sub>4</sub><sup>4-</sup>) ions [4–6]. The substitution or inclusion of these minor ions in HA changes its morphology, crystalline structure and physicochemical properties [7], leading to the enhanced bioactivity [8,9]. Among them, the important ions in the synthetic HA for biological applications are the SiO<sub>4</sub><sup>4-</sup> and CO<sub>3</sub><sup>2-</sup> ions since the mineral bone contains substantial amounts of the ions [10]. In biological bones, the contents of CO<sub>3</sub><sup>2-</sup> and SiO<sub>4</sub><sup>4-</sup> ions are approximately 4–8 wt% [8,11] and 0.4–0.5 wt% [12,13], respectively. The SiO<sub>4</sub><sup>4-</sup> ions (e.g., silicate ion) are indispensable in the early stages of bone and cartilage formation, since they promote the mineralization, contributing to proper osteointegration and helping to bond the implanted material with the biological bone [9,14]. Thus, the incorporation of silicate ions in the HA structure can significantly improve the biological reactivity of HA [15]. On the other hand, the PO<sub>4</sub><sup>3-</sup> ions of HA can be substituted by the CO<sub>3</sub><sup>2-</sup> ions, generating the B-type carbonated hydroxyapatite (CHA) [16,17]. The B-type CHA has greater solubility, subserving the Ca<sup>2+</sup> and PO<sub>4</sub><sup>3-</sup> ion concentration, which favours the osteointegration [18,19]. Furthermore, CHA enhances the osteoclast resorption allowing new bone formation [20,21]. Therefore, the understanding of the inclusion of silicate and carbonate ions in HA is the basis for effective control of the bioactivity. Although

diverse studies have been carried out on the substitution of carbonate and silicate ions in HA [22], the mechanism of substitution and/or inclusion in low-crystalline HA has not been completely clarified [23–25].

The aim of this study is to control the simultaneous incorporation of  $\text{SiO}_4^{4-}$  and  $\text{CO}_3^{2-}$  ions into HA to obtain low-crystalline HA particles (SiHA) under the presence of sodium silicate in order to increase the HA bioreactivity. The preparation conditions are similar to the physiological conditions used to obtain the particles that are close to the biological HA. The mechanism of substitution with  $\text{SiO}_4^{4-}$  and  $\text{CO}_3^{2-}$  ions in the HA particles was investigated using the Fourier transform infrared spectrometer, X-ray diffraction, field emission scanning electron microscope, and solid-state  $^{29}\text{Si}$ -NMR spectra recorded by dipolar decoupled magic-angle spinning.

## 2. Materials and Methods

The SiHA particles with the assumed formula of  $\text{Ca}_{10}(\text{PO}_4)_{6-x}(\text{SiO}_4)_x(\text{OH})_{2-x}$  ( $x = 0\text{--}8.0$ ,  $\text{Ca}/(\text{P} + \text{Si}) = 1.67$ ) were synthesized. Dipotassium hydrogen phosphate ( $\text{K}_2\text{HPO}_4$ , FUJIFILM Wako Pure Chemical Co. (Osaka, Japan), purity: 99.0+ wt%), sodium silicate (Water glass,  $\text{Na}_2\text{O}\cdot 2\text{SiO}_2$  with molar ratio ( $\text{SiO}_2/\text{Na}_2\text{O}$ ): 2.06–2.31, FUJIFILM Wako Pure Chemical Co. (Osaka, Japan)), and calcium chloride dihydrate ( $\text{CaCl}_2\cdot 2\text{H}_2\text{O}$ , FUJIFILM Wako Pure Chemical Co. (Osaka, Japan), purity: 99.0–103.0 wt%) were used as the starting reagents. The theoretical silicon concentration in SiHA was set at 0, 0.8, 1.5, 4.0, 6.0 and 8.0 wt%. The detailed initial addition amounts were listed in ESM, Table S1. The required amount of  $\text{K}_2\text{HPO}_4$  and  $\text{Na}_2\text{O}\cdot 2\text{SiO}_2$  were dissolved in deionized water (0.04 L) at 60 °C. Then, the deionized water (0.02 L) containing  $\text{CaCl}_2\cdot 2\text{H}_2\text{O}$  (0.01 mol) was added to the phosphate and silicate ion solution with continuous stirring at 60 °C. Then, the pH level was adjusted to be 13, and the solution was stirred at 80 °C. After centrifugation, the solid product was washed with ultrapure water and dried at 65 °C for 24 h, and then heated at 250 °C for 3 h. The samples were named as HA, 0.8SiHA, 1.5SiHA, 4.0SiHA, 6.0SiHA and 8.0SiHA depending on the feed Si concentration.

The characterization was performed by using Fourier transform infrared (FT-IR) spectrometer, wavelength dispersive X-ray fluorescence (XRF) spectrometer, X-ray diffraction (XRD), field emission scanning electron microscope (FE-SEM), and solid-state  $^{29}\text{Si}$ -nuclear magnetic resonance recorded by dipolar decoupled magic-angle spinning ( $^{29}\text{Si}$ -NMR DD-MAS). Based on the FT-IR spectra methodology, the quantification of  $\text{CO}_3^{2-}$  ions (wt%) was performed by the relative absorbance area ratio of  $\nu_1\text{CO}_3^{2-}$  ( $1570\text{--}1330\text{ cm}^{-1}$ ) to  $\nu_1\nu_3\text{PO}_4^{3-}$  ( $\sim 900\text{--}1230\text{ cm}^{-1}$ ) [26]. According to Scherer's equation ( $K = 0.89$ ), crystalline size along the  $a$ -axis ( $D_{300}$ ) was calculated from the half width of the  $D_{300}$  diffraction patterns in the XRD. In the solid state  $^{29}\text{Si}$ -NMR spectra, the chemical shift was adjusted by referencing the peak position of tetramethylsilane, and was evaluated by the spectral separation technique based on the peaks of  $Q_0$  ( $-72 \pm 2$  ppm) due to isolated silicon unit,  $Q_1$  ( $-74 \pm 2$  ppm) due to one Si–O–Si and three Si–OH bonds [27] and  $Q_2$  ( $-90 \pm 2$  ppm) due to two Si–O–Si and two Si–OH bonds [28].

## 3. Results and Discussion

The Si concentrations obtained by XRF were 0.4, 0.7, 3.3, 5.0 and 6.9 wt% for 0.8SiHA, 1.5SiHA, 4.0SiHA, 6.0SiHA and 8.0SiHA. As shown in Figure 1a, the Ca/P molar ratio in the SiHA particles increased with the increase in feed Si concentration, suggesting the substitutions of  $\text{PO}_4^{3-}$  with  $\text{SiO}_4^{4-}$  ions in the HA. Due to the ion substitution, the amount of  $\text{PO}_4^{3-}$  ions decreased, causing an increase in the Ca/P molar ratio [18]. On the other hand, the Ca/(Si + P) molar ratio only decreased slightly with the increase in the feeding of Si, indicating the inclusion of  $\text{SiO}_4^{4-}$  ions in the HA.

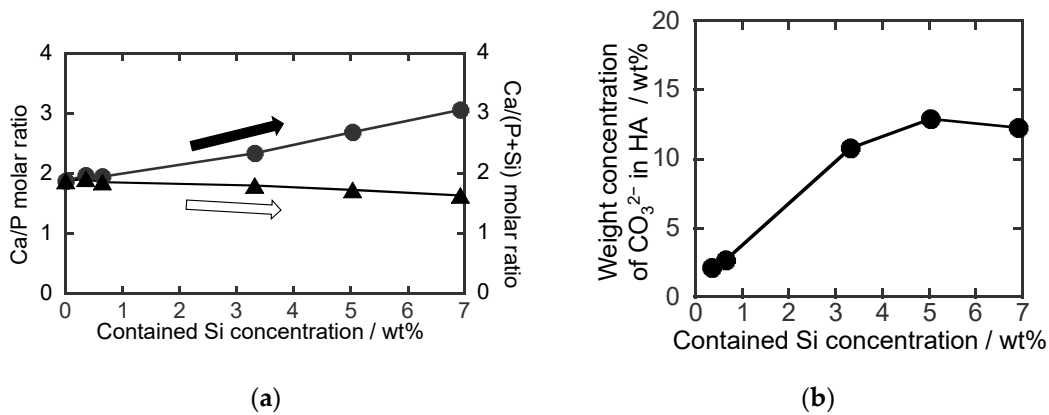
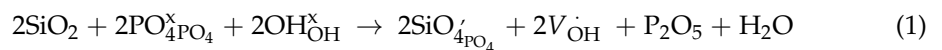


**Figure 1.** (a) Resultant molar ratios of the (●) Ca to P (Ca/P) and the (▲) Ca to (P + Si) (Ca/(P + Si)) and (b) carbonate weight concentration in the SiHA particles. Here, the contained Si concentrations were 0.35, 0.65, 3.32, 5.03 and 6.92 wt% for 0.8SiHA, 1.5SiHA, 4.0SiHA, 6.0SiHA and 8.0SiHA.

The FT-IR spectra of the SiHA particles (Figure S1) show the stretching vibration band of  $\nu_1(\text{PO}_4^{3-})$  ions at  $960\text{ cm}^{-1}$ . The band assigned to Si-OH vibrational modes of  $\text{SiO}_4^{4-}$  ions appears at  $890\text{ cm}^{-1}$ . The P-O stretching vibration bands of  $\text{PO}_4^{3-}$  ions ( $1100, 1045\text{ cm}^{-1}$ ) and the Si-O-Si asymmetric bands of  $\text{SiO}_4^{4-}$  ions ( $1040\text{--}1200\text{ cm}^{-1}$ ) are located very close, which makes interpretation difficult. The bands at around  $1470, 1550\text{ cm}^{-1}$  correspond to the asymmetric stretching mode of  $\nu_3\text{CO}_3^{2-}$  ions. The band at  $\sim 3570\text{ cm}^{-1}$  is assigned to the  $\text{OH}^-$  stretching mode [29–32]. It was observed that the increase in Si concentration caused an increase in the intensity of the Si-OH band and a decrease in the intensity of the  $\nu_1(\text{PO}_4^{3-})$  band, corroborating the inclusion of  $\text{SiO}_4^{4-}$  ions by the substitution of  $\text{PO}_4^{3-}$  ions. Furthermore, increasing the Si concentration increased the intensity of the  $\text{CO}_3^{2-}$  bands, indicating the simultaneous substitution of  $\text{PO}_4^{3-}$  ions with  $\text{SiO}_4^{4-}$  and  $\text{CO}_3^{2-}$  ions in the HA to form SiHA. This can be described by the possible formula (e.g.,  $2\text{PO}_4^{3-} \rightarrow \text{SiO}_4^{4-} + \text{CO}_3^{2-}$ ) [33]. The incorporation of  $\text{SiO}_4^{4-}$  ions caused a decrease in the intensity of the  $\text{OH}^-$  band until it almost disappeared in 8.0SiHA, implying the loss of  $\text{OH}^-$  ions to compensate for the excess negative charges generated by the substitution of the  $\text{PO}_4^{3-}$  ions with more negative ions ( $\text{SiO}_4^{4-}$ ). Using the Kröger-Vink notation [34], the charge compensation mechanism [35] can be expressed as follows:



Therefore, the increase in Si concentration effectively caused an increase in the content of  $\text{CO}_3^{2-}$  ions, as shown in Figure 1b, indicating that the presence of  $\text{SiO}_4^{4-}$  ions induced the inclusion of  $\text{CO}_3^{2-}$  ions in HA. The incorporation of  $\text{SiO}_4^{4-}$  and  $\text{CO}_3^{2-}$  ions into HA increased the defects in the HA structure, resulting in more vacancies of  $\text{OH}^-$  ( $V_{\text{OH}}^{\cdot}$ ) due to more substitutions of  $\text{PO}_4^{3-}$  ions. The simultaneous substitution of the  $\text{PO}_4^{3-}$  ions in the HA with  $\text{SiO}_4^{4-}$  and  $\text{CO}_3^{2-}$  ions can be described as follows [13,36]

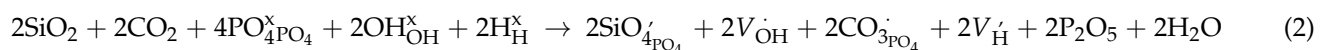
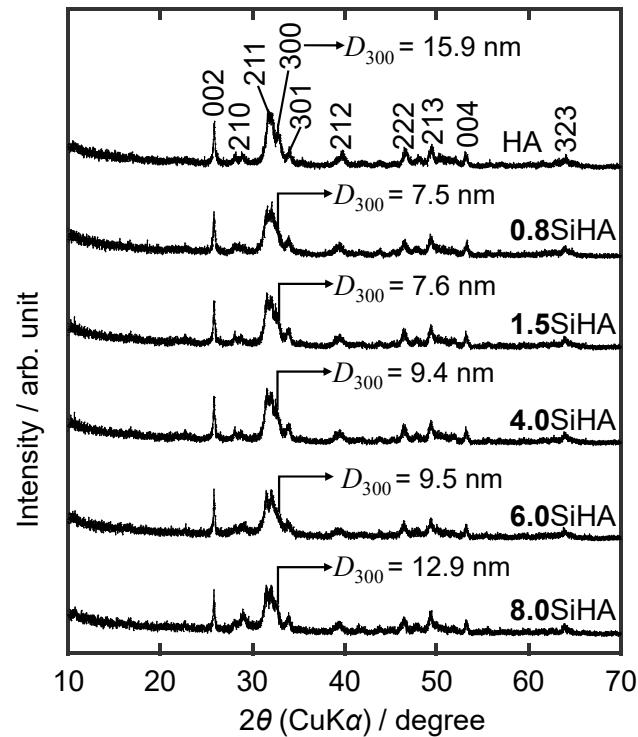


Figure 2 shows the XRD patterns of HA and SiHA particles at the different Si concentrations. All the patterns were ascribed to a HA ( $\text{Ca}_{10}(\text{PO}_4)_6(\text{OH})_2$ , ICDD: 00-009-0432). It was observed that the increase in Si concentration resulted in a decrease in crystallinity, which was caused by the defects and the formation of  $V_{\text{OH}}^{\cdot}$  due to the substitution of  $\text{PO}_4^{3-}$  ions with  $\text{SiO}_4^{4-}$  and  $\text{CO}_3^{2-}$  ions in the HA structure. The calculated  $D_{300}$  crystalline sizes along with the  $a$ -axis of all the SiHA samples were smaller than the HA (Figure 2 (inset)) due to the incorporation of  $\text{SiO}_4^{4-}$  and  $\text{CO}_3^{2-}$  ions into the HA structure [37]. It was observed that the value of  $D_{300}$  first decreased (0.8SiHA) and then began to increase with increasing the Si concentration. Especially, 8.0SiHA had the highest value of  $D_{300}$ , suggesting

that the substitution of  $\text{PO}_4^{3-}$  ions with  $\text{SiO}_4^{4-}$  ions would occur predominantly, since the radius of the  $\text{Si}^{4+}$  (0.042 nm) is greater than that of  $\text{P}^{5+}$  (0.035 nm), and the bond length of the Si–O bond (0.16 nm) is greater than that of the P–O bond (0.15 nm) [20,38], which must result in a higher  $D_{300}$  value. These results are consistent with the crystal sizes observed in FE-SEM images (Figure S2). In the images, all the SiHA particles exhibit needle-like shapes with the smaller sizes than HA, and the aggregation forms were observed.



**Figure 2.** XRD patterns of the HA and SiHA particles (Inset:  $D_{300}$  values).

Figure 3a shows the deconvolution curves and fitting results of the spectra of the SiHA particles provided by their  $Q_0$ – $Q_2$  components. At the lower Si concentration (0.8SiHA and 1.5SiHA), only  $Q_0$  peak was observed. However, at the higher Si concentration (4.0SiHA, 6.0SiHA and 8.0SiHA), the  $Q_1$  and  $Q_2$  peaks appeared. The  $Q_0$  peak of the  $\text{SiO}_4$  tetrahedron corresponded to the stretching Si–O band in the FT-IR spectra of SiHA. The possible inclusion mechanism of the silicates ions into HA structure is shown in Figure 3b. It was suggested that the substitution with  $\text{SiO}_4^{4-}$  ions in the HA structures was related to the inclusion of  $\text{CO}_3^{2-}$  ions, which was proposed by the reaction mechanism based on the substitution of phosphate ions in Figure 3(b-1). Polymerized silicate chains (e.g., oligomeric silicates) due to  $Q_1$  and  $Q_2$  peaks appeared at the Si concentration of 3.32 wt%, suggesting that the unsubstituted  $\text{SiO}_4^{4-}$  ions began to adsorb on the SiHA with the polymerization and condensation reactions. At the Si concentrations of 5.03 and 6.92 wt%, the intensities of  $Q_1$  and  $Q_2$  increased, suggesting that the unsubstituted  $\text{SiO}_4^{4-}$  ions started to form oligomeric fragments and adsorbed on the SiHA. These results indicated that the oligomeric fragments are larger in the presence of more unsubstituted  $\text{SiO}_4^{4-}$  ions as shown in Figure 3(b-2).

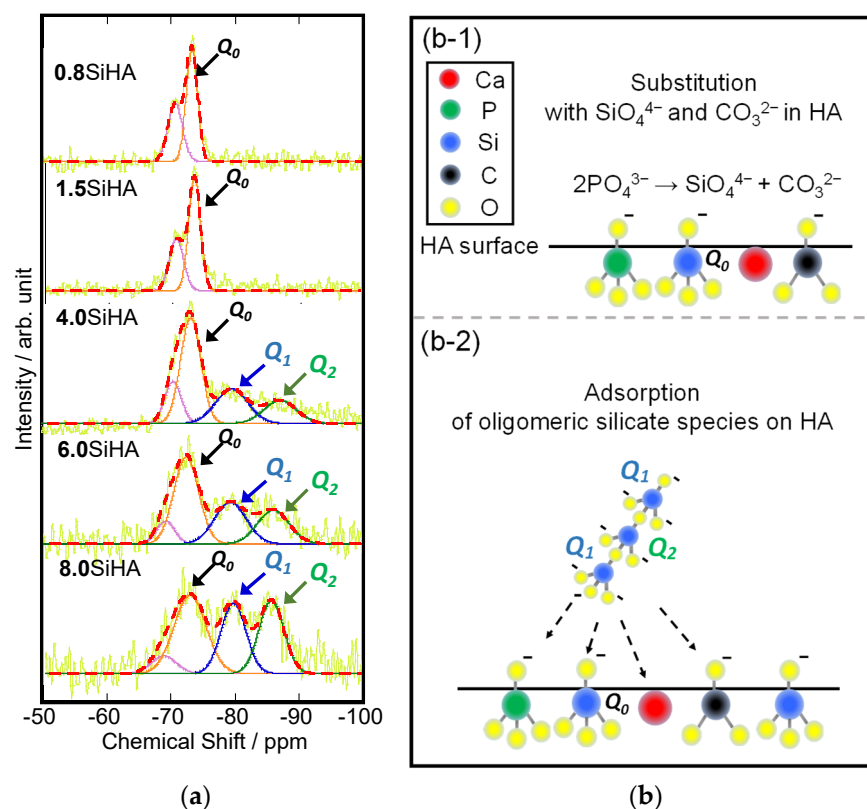


**Figure 3.** (a) Deconvolution curves (red dotted lines) and fitting results (coloured lines) of solid-state  $^{29}\text{Si}$ -NMR DD-MAS spectra of the SiHA particles with the  $Q_n$  ( $n = 0, 1, 2$ ) derived from raw data (yellow lines). Schemes of the possible states of carbonate and silicate ions at the HA surfaces for the case in (b-1) 0.8SiHA and 1.5SiHA and (b-2) 4.0SiHA, 6.0SiHA and 8.0SiHA. The increment in the Si concentration increases the relative  $Q_2$  peak intensity, suggesting the absorption of oligomer derived from unsubstituted silicate ions on the HA surface.

#### 4. Conclusions

The inclusion of both silicate and carbonate ions was successfully achieved in the presence of sodium silicate. The content of silicate ions increased with increasing Si feed. The silicate ions promoted the inclusion of carbonate ions in the HA. The substitution of phosphate ions with silicate and carbonate ions into the HA structure produced defects and hydroxyl vacancies, generating a loss in crystallinity and smaller crystalline sizes. The substitution of phosphate ions was mainly dominated with silicate ions in the structure, inducing the particle growth along with the  $a$ -axis. The results of solid-state  $^{29}\text{Si}$ -NMR DD-MAS demonstrated that at the lower Si feed, only ion substitution has occurred. At the higher Si content, the remaining silicate ions with the saturation of substitution formed the (poly)silicate species (i.e., oligomeric silicates). It was observed that these (poly)silicate species have a strong tendency to adsorb to the HA surfaces, modulating the crystal growth of the SiHA. Thus, the solid state  $^{29}\text{Si}$ -NMR spectra indicated that upon reaching saturation in the substitution of phosphate ions with silicate ions, the remaining silicate ions polymerized to form (poly)silicate species adsorbed on the surface of the HA, suggesting the appearance of the silicate surface layer on the SiHA surfaces. There is a possibility to control the silicate ion states, the inclusion amount of carbonate ions in SiHA and its crystalline size by the feed concentration of sodium silicate. The incorporation of silicate and carbonate ions into the HA structure is expected to enhance the bioactivity of the SiHA particles.

**Supplementary Materials:** The following supporting information can be downloaded at: <https://www.mdpi.com/article/10.3390/biomimetics7020040/s1>, Table S1: Added amounts of the reagents

in the synthesis of the SiHA particles; Figure S1: FT-IR spectra of the HA and SiHA particles; Figure S2: FE-SEM images of the HA and SiHA particles.

**Author Contributions:** Conceptualization, T.G.P.G., K.S., S.Y., T.S. and M.T.; methodology, K.S., S.Y. and T.S.; software, K.S. and T.S.; validation, K.S., S.Y., Z.L., M.T. and T.G.P.G.; formal analysis, T.S., T.G.P.G. and Z.L.; investigation, T.G.P.G.; resources, M.T.; data curation, K.S. and T.S.; writing—original draft preparation, T.G.P.G.; writing—review and editing, Z.L. and M.T.; supervision, M.T.; project administration, M.T. All authors have read and agreed to the published version of the manuscript.

**Funding:** This research received no external funding.

**Institutional Review Board Statement:** Not applicable.

**Informed Consent Statement:** Not applicable.

**Data Availability Statement:** Data available on request from the authors.

**Acknowledgments:** The authors would like to thank Analysis and Instrumentation Center in Nagoya University of Technology for providing their facilities.

**Conflicts of Interest:** The authors declare no conflict of interest.

## References

1. Palard, M.; Champion, E.; Foucaud, S. Synthesis of silicated hydroxyapatite  $\text{Ca}_{10}(\text{PO}_4)_{6-x}(\text{SiO}_4)_x(\text{OH})_{2-x}$ . *J. Solid State Chem.* **2008**, *181*, 1950–1960. [[CrossRef](#)]
2. Solonenko, A.P. Biomaterials based on mixtures of calcium phosphates and silicates: Investigation of possible production by precipitation from water solutions. *Glas. Ceram.* **2017**, *73*, 386–389. [[CrossRef](#)]
3. Galindo, T.G.P.; Chai, Y.; Tagaya, M. Hydroxyapatite nanoparticle coating on polymer for constructing effective biointeractive interfaces. *J. Nanomater.* **2019**, *2019*, 6495239. [[CrossRef](#)]
4. Posner, A.S.; Betts, F. Synthetic Amorphous Calcium Phosphate and Its Relation to Bone Mineral Structure. *Acc. Chem. Res.* **1975**, *8*, 273–281. [[CrossRef](#)]
5. Patel, K.D.; Singh, R.K.; Lee, J.H.; Kim, H.W. Electrophoretic coatings of hydroxyapatite with various nanocrystal shapes. *Mater. Lett.* **2019**, *234*, 148–154. [[CrossRef](#)]
6. Singh, R.K.; Kim, T.H.; Patel, K.D.; Kim, J.J.; Kim, H.W. Development of biocompatible apatite nanorod-based drug-delivery system with in situ fluorescence imaging capacity. *J. Mater. Chem. B* **2014**, *2*, 2039–2050. [[CrossRef](#)]
7. Solonenko, A.P.; Golovanova, O.A. Silicate-substituted carbonated hydroxyapatite powders prepared by precipitation from aqueous solutions. *Russ. J. Inorg. Chem.* **2014**, *59*, 1228–1236. [[CrossRef](#)]
8. Solonenko, A.P.; Blesman, A.I.; Polonyankin, D.A.; Bel'skaya, L.V. Effect of sodium silicate on the nature of crystallization products in calcium phosphate systems. *Russ. J. Inorg. Chem.* **2017**, *62*, 1286–1292. [[CrossRef](#)]
9. Sindu, P.A.; Kolanthai, E.; Suganthi, R.V.; Arul, K.T.; Manikandan, E.; Catalani, L.H.; Kalkura, S.N. Green synthesis of Si-incorporated hydroxyapatite using sodium metasilicate as silicon precursor and in vitro antibiotic release studies. *J. Photochem. Photobiol. B Biol.* **2017**, *175*, 163–172. [[CrossRef](#)]
10. Boanini, E.; Gazzano, M.; Bigi, A. Ionic substitutions in calcium phosphates synthesized at low temperature. *Acta Biomater.* **2010**, *6*, 1882–1894. [[CrossRef](#)]
11. Tagaya, M.; Ikoma, T.; Takeguchi, M.; Hanagata, N.; Tanaka, J. Interfacial serum protein effect on biological apatite growth. *J. Phys. Chem. C* **2011**, *115*, 22523–22533. [[CrossRef](#)]
12. Sprio, S.; Tampieri, A.; Landi, E.; Sandri, M.; Martorana, S.; Celotti, G.; Logroscino, G. Physico-chemical properties and solubility behaviour of multi-substituted hydroxyapatite powders containing silicon. *Mater. Sci. Eng. C* **2008**, *28*, 179–187. [[CrossRef](#)]
13. Gibson, I.R.; Best, S.M.; Bonfield, W. Chemical characterization of silicon-substituted hydroxyapatite. *J. Biomed. Mater. Res.* **1999**, *44*, 422–428. [[CrossRef](#)]
14. Hijón, N.; Cabañas, M.V.; Peña, J.; Vallet-Regí, M. Dip coated silicon-substituted hydroxyapatite films. *Acta Biomater.* **2006**, *2*, 567–574. [[CrossRef](#)]
15. Xu, J.L.; Khor, K.A. Chemical analysis of silica doped hydroxyapatite biomaterials consolidated by a spark plasma sintering method. *J. Inorg. Biochem.* **2007**, *101*, 187–195. [[CrossRef](#)]
16. Suetsugu, Y.; Takahashi, Y.; Okamura, F.P.; Tanaka, J. Structure Analysis of A-Type Carbonate Apatite by a Single-Crystal X-ray Diffraction Method. *J. Solid State Chem.* **2000**, *155*, 292–297. [[CrossRef](#)]
17. Fleet, M.E.; Liu, X. Coupled substitution of type A and B carbonate in sodium-bearing apatite. *Biomaterials* **2007**, *28*, 916–926. [[CrossRef](#)]
18. Bang, L.T.; Long, B.D.; Othman, R. Carbonate hydroxyapatite and silicon-substituted carbonate hydroxyapatite: Synthesis, mechanical properties, and solubility evaluations. *Sci. World J.* **2014**, *2014*, 969876. [[CrossRef](#)]

19. Ibrahim, D.M.; Mostafa, A.A.; Korowash, S.I. Chemical characterization of some substituted hydroxyapatites. *Chem. Cent. J.* **2011**, *5*, 74. [[CrossRef](#)]
20. Bang, L.T.; Ramesh, S.; Purbolaksono, J.; Ching, Y.C.; Long, B.D.; Chandran, H.; Othman, R. Effects of silicate and carbonate substitution on the properties of hydroxyapatite prepared by aqueous co-precipitation method. *Mater. Des.* **2015**, *87*, 788–796. [[CrossRef](#)]
21. Reffitt, D.M.; Ogston, N.; Jugdaohsingh, R.; Cheung, H.F.J.; Evans, B.A.J.; Thompson, R.P.H.; Powell, J.J.; Hampson, G.N. Orthosilicic acid stimulates collagen type 1 synthesis and osteoblastic differentiation in human osteoblast-like cells in vitro. *Bone* **2003**, *32*, 127–135. [[CrossRef](#)]
22. Ratnayake, J.T.B.; Mucalo, M.; Dias, G.J. Substituted hydroxyapatites for bone regeneration: A review of current trends. *J. Biomed. Mater. Res. Part B Appl. Biomater.* **2016**, *105*, 1285–1299. [[CrossRef](#)] [[PubMed](#)]
23. Biedrzycka, A.; Skwarek, E.; Hanna, U.M. Hydroxyapatite with magnetic core: Synthesis methods, properties, adsorption and medical applications. *Adv. Colloid Interface Sci.* **2021**, *291*, 102401. [[CrossRef](#)] [[PubMed](#)]
24. Skwarek, E.; Gładysz-Płaska, A.; Choromańska, J.B.; Broda, E. Adsorption of uranium ions on nano-hydroxyapatite and modified by Ca and Ag ions. *Adsorption* **2019**, *25*, 639–647. [[CrossRef](#)]
25. Skwarek, E.; Gładysz-Płaska, A.; Bolbukh, Y. Adsorption of Uranyl Ions at the Nano-hydroxyapatite and Its Modification, Nanosca. *Res. Lett.* **2017**, *12*, 278.
26. Grunenwald, A.; Keyser, C.; Sautereau, A.M.; Crubézy, E.; Ludes, B.; Drouet, C. Revisiting carbonate quantification in apatite (bio)minerals: A validated FTIR methodology. *J. Archaeol. Sci.* **2014**, *49*, 134–141. [[CrossRef](#)]
27. Tagaya, M.; Abe, S.; Motozuka, S.; Shiba, K.; Takemura, T.; Hayashi, I.; Sakaguchi, Y. Surface-engineered mesoporous silica particles with luminescent, cytocompatible and targeting properties for cancer cell imaging. *RSC Adv.* **2017**, *7*, 13643–13652. [[CrossRef](#)]
28. Yamada, S.; Tagaya, M.; Yamada, S.; Motozuka, S. Synthesis of nanostructured silica/hydroxyapatite hybrid particles containing amphiphilic triblock copolymer for effectively controlling hydration layer structures with cytocompatibility. *J. Mater. Chem. B* **2020**, *8*, 1524–1537. [[CrossRef](#)]
29. Koutsopoulos, S. Synthesis and characterization of hydroxyapatite crystals: A review study on the analytical methods. *J. Biomed. Mater. Res.* **2002**, *62*, 600–612. [[CrossRef](#)]
30. Aminian, A.; Solati-Hashjin, M.; Samadikuchaksaraei, A.; Bakhshi, F.; Gorjipour, F.; Farzadi, A.; Moztarzadeh, F.; Schmücker, M. Synthesis of silicon-substituted hydroxyapatite by a hydrothermal method with two different phosphorous sources. *Ceram. Int.* **2011**, *37*, 1219–1229. [[CrossRef](#)]
31. Antonakos, A.; Liarokapis, E.; Leventouri, T. Micro-Raman and FTIR studies of synthetic and natural apatites. *Biomaterials* **2007**, *28*, 3043–3054. [[CrossRef](#)] [[PubMed](#)]
32. Hayakawa, S.; Kanaya, T.; Tsuru, K.; Shirosaki, Y.; Osaka, A.; Fujii, E.; Kawabata, K.; Gasqueres, G.; Bonhomme, C.; Babonneau, F.; et al. Heterogeneous structure and in vitro degradation behavior of wet-chemically derived nanocrystalline silicon-containing hydroxyapatite particles. *Acta Biomater.* **2013**, *9*, 4856–4867. [[CrossRef](#)] [[PubMed](#)]
33. Mostafa, N.Y.; Hassan, H.M.; Abd Elkader, O.H. Preparation and Characterization of Na<sup>+</sup>, SiO<sub>4</sub><sup>4-</sup>, and CO<sub>3</sub><sup>2-</sup> Co-Substituted Hydroxyapatite. *J. Am. Ceram. Soc.* **2011**, *94*, 1584–1590. [[CrossRef](#)]
34. Kröger, F.A.; Vink, H.J. Relations between the Concentrations of Imperfections in Crystalline Solids. *Solid State Phys.* **1956**, *3*, 307–435.
35. Targonska, S.; Wiglusz, R.J. Investigation of physicochemical properties of the structurally modified nanosized silicate-substituted hydroxyapatite co-doped with eu<sup>3+</sup> and sr<sup>2+</sup> ions. *Nanomaterials* **2021**, *11*, 27. [[CrossRef](#)]
36. Gibson, I.R.; Bonfield, W. Novel synthesis and characterization of an AB-type carbonate-substituted hydroxyapatite. *J. Biomed. Mater. Res.* **2001**, *59*, 697–708. [[CrossRef](#)] [[PubMed](#)]
37. Pietak, A.M.; Reid, J.W.; Stott, M.J.; Sayer, M. Silicon substitution in the calcium phosphate bioceramics. *Biomaterials* **2007**, *28*, 4023–4032. [[CrossRef](#)] [[PubMed](#)]
38. Tang, X.L.; Xiao, X.F.; Liu, R.F. Structural characterization of silicon-substituted hydroxyapatite synthesized by a hydrothermal method. *Mater. Lett.* **2005**, *59*, 3841–3846. [[CrossRef](#)]